Design of an Efficient Non-Backdrivable Mechanism with Wrap Spring for Hand Prosthesis

Côme Butin, Yannick Aoustin, David Gouaillier, Damien Chablat

Côme Butin
Nantes Université, École Centrale Nantes,
CNRS, LS2N, UMR 6004,
44000 Nantes, France
& ORTHOPUS
Assistive technology manufacturer
Nantes, FRANCE
email: come.butin@orthopus.com

Yannick Aoustin
Nantes Université, École Centrale Nantes,
CNRS, LS2N, UMR 6004,
44000 Nantes, France
email: yannick.aoustin@univ-nantes.fr

David Gouaillier
ORTHOPUS,
Assistive technology manufacturer
Nantes, FRANCE
email: david.gouaillier@orthopus.com

Damien Chablat[1]
Nantes Université, École Centrale Nantes,
CNRS, LS2N, UMR 6004,
44000 Nantes, France
Technical University of Cluj-Napoca,
Romania
email: damien.chablat@cnrs.fr

Design of an Efficient Non-backdrivable Mechanism with Wrap Spring for Hand Prosthesis

The aim of this article is to create a system that enables power transmission non-backdrivability in a hand prosthesis with a single actuator. This system allows the motor to be stopped while maintaining the gripping force to prevent the held object from being dropped. This non-backdrivability allows users, for example, to release muscle contractions while still keeping a tight grip on an object, as well as completely turning off the prosthesis to avoid unintentional commands that could lead to loosening the object. Beyond the functional aspect of non-backdrivability, the physical non-backdrivability of the transmission enables the full power of the motors to be utilized without exceeding their thermal limits. To be effectively used, the non-backdrivable system must be energy efficient. A state-of-the-art analysis of different non-backdrivable mechanisms is conducted, evaluating their functioning and maximum efficiency. A novel system is developed based on an existing principle but with a focus on simplicity of manufacturing and fewer components compared to existing systems. An analysis is conducted to understand the effect of each mechanism parameter, and a dimensioning procedure is derived. A prototype is developed to compare theoretical values with measured values. The obtained results are analyzed and discussed.

Keywords: Hand prosthesis, Motion transmission, Non-backdrivable mechanism.

1 Introduction

Developing assistive hand prostheses for individuals in need presents significant challenges. Over the years, myoelectric prostheses have been at the forefront of these advancements. Early designs featured a single degree of actuation (DoA) to prioritize simplicity and durability, with the tridigital grasp or opposite pinch being the primary grasping mode. Some of these tridigital prostheses, like the *VariPlus Speed* (Ottobock), are still available today, while newer models like the *Myo Kinisi* (Steeper Group) were introduced in 2021. Meanwhile, more sophisticated prostheses with articulated phalanxes and up to six actuators are currently on the market, including the *i-Limb* (Össur/Touch Bionics), the *Bebionic hand* (Ottobock), the *TASKA hand* (TASKA Prothetics), and the *COVVI hand* (COVVI). These advanced models can perform a diverse array of grip patterns, enhancing their utility for users.

Most of the research efforts focus on the functionality of the prosthetic hand, that is its capacity to realize different grasping patterns and adapt it to the objects. However, performances of the hand such as closing speed and grasping force are important, and users report a lack of performance in current prostheses [1]. If not correctly optimized, power transmission can lead to poor performances or require too large and heavy motors. Optimizing power transmission also benefits the energy capacity of the prosthesis.

Several components of the power transmission permit to obtain better performances, such as a Load Adaptive Variable Transmission (LAVT) presented in a previous work [2]. This type of mechanism is used in the *VariPlus Speed*, where a lot of efforts have been deployed to optimize its power transmission, leading to the most powerful prosthetic hand currently on the market. Other components are used such as Non-BackDrivable Mechanism (NBDM). Non-backdrivability is an important property of the power transmission, while it allows holding an object without any torque from the motor, thus permitting to turn off the prosthetic to prevent unwanted movements during a specific task or to avoid energy loss in the motor producing heat.

In most of the poly-articulated prostheses where one motor and its transmission is used for each finger, a worm drive or a screw nut transmission is used [3]. These systems are well known and easy to integrate, realizing speed reduction and non-backdrivability in a single system. However, their working principle does not permit them to achieve both non-backdrivability and good efficiency, thus leading to 55 to 70% power loss in this single component.

Controzzi *et al* have developed a roller based NBDM [4,5] with an efficiency up to 95%. If this mechanism meets the functionalities needed for a NBDM and could be used in a commercial prosthesis, it also carries drawbacks. Authors underline the wear effect of the contact surfaces, that need maintenance. Such a mechanism also requires accurate CNC machining which increases the cost of such a mechanism. Finally, it is composed of a lot of tiny parts such as rollers and springs that increase complexity and lower maintenance ease.

To realize the non-backdrivability property in its tridigital myoelectric hands while keeping efficient power transmission, Ottobock has developed a wrap spring-based NBDM. This mechanism is well optimized and its compacity is impressive. However, the mechanism is built from tiny plastic parts that are a source of weakness, and its design requires over-molding and mass production tools, not adapted for small-scale manufacturing.

In this study, we propose a new efficient wrap spring-based NBDM. While taking advantage of the wrap spring as used by Ottobock, it proposes a simpler design, using the spring as the only moving part between the input and the output shaft. The spring geometry is developed to minimize friction loss while ensuring fingers lock when the motor is cut off. The output backlash of the mechanism can also be minimized during the design process. The proposed mechanism can be adapted to different torque requirements depending on the integration constraints.

[1]Corresponding Author.
Version 1.18, April 4, 2024

This work was conducted in collaboration with the BionicoHand project [6], which aims to develop an accessible Open Source[2] prosthesis. This prosthetic hand is composed of rigid fingers (with no interphalangeal joint) and one single actuator to realize both opposite and lateral grasps [7]. However, the solution proposed in this paper is also adapted for any prosthetic hand or robotic gripper transmission requiring both high power and low energy consumption.

This paper is outlined as follows. A state-of-the-art of existing non-backdrivable mechanisms is proposed in Sec. 2, and the working principle of each solution is detailed. Then, a new concept of a non-backdrivable mechanism based on a wrap spring is presented in Sec. 3. A complete procedure that permits to size of the mechanism according to specifications is detailed in Sec. 4. Then, Sec. 5 presents the experimental setup and the corresponding results that validate the working principle of such a mechanism. Finally, Sec. 6 offers conclusions and directions for future work.

2 State of the Art of Existing Non-backdrivable Mechanisms

2.1 Function and Different Types of Non-backdrivable Mechanisms. A non-backdrivable mechanism is a mechanism that allows transmitting the motion from an input mechanical element to an output load (rotational mode) but blocks any movement of the output load when the input element is left free (blocking mode). The non-backdrivability of a mechanism may or may not be desired. In particular, high-ratio reducers can sometimes be considered non-backdrivable because of the significant effort required to move the output shaft when the input is left free. In the case of a hand prosthesis, controlled and systematic non-backdrivability is desired to maintain maximum gripping force at the fingertips while the input is left free. Therefore, a specific mechanism is sought to achieve this function. In this way, energy consumption will be significantly reduced.

To achieve this function, one of the first ideas is to use an active system that can actuate a locking or braking element on the transmission. Many mechanisms exist and are used in robotics [8]. Many manipulator arms use electromagnetic brakes or linear solenoids. Claw clutches, ratchet wheels, and piezoelectric brakes are also used.

However, there are passive solutions to achieve this function, such as worm drives used in many poly articulated prostheses [3], or other mechanisms closer to clutches in the broad sense. In particular, some non-backdrivable mechanisms are strongly inspired by freewheeling technologies used in many mechanical systems.

Four different principles have been identified in various prostheses and are analyzed in the following sections.

2.2 Worm Drive. The best-known non-backdrivable mechanisms are worm drives and screw-nut systems. The two mechanisms differ only in the output motion, rotational for the first and translational for the second. Both mechanisms are based on the same principle: when the screw is driven, the output gear or nut is forced to move but slides on the screw's threads, creating friction losses. When the thread's inclination angle β, also known as the helix angle, is sufficiently small, the friction becomes significant. In particular, by modeling the forces on the teeth, it can be shown that the system becomes non-backdrivable when the helix angle β is smaller than the friction cone angle φ such that $\mu = \tan\varphi$, where μ is the coefficient of friction. This leads to $\tan\varphi > \tan\beta$, or equivalently $\mu/\tan\beta > 1$.

The mechanical efficiency η of this system is low. Denoting α_n as the pressure angle of the teeth, this efficiency is calculated by the formula [9]:

$$\eta = \frac{\cos\alpha_n - \mu\tan\beta}{\cos\alpha_n + \frac{\mu}{\tan\beta}} = \frac{\cos\alpha_n}{\cos\alpha_n + \frac{\mu}{\tan\beta}} - \frac{\mu\tan\beta}{\cos\alpha_n + \frac{\mu}{\tan\beta}} \quad (1)$$

Using the non-backdrivability relation $\mu/\tan\beta > 1$ and noting that $\cos\alpha_n < 1$, we can estimate an upper bound on the efficiency:

$$\eta < \frac{\cos\alpha_n}{\cos\alpha_n + \frac{\mu}{\tan\beta}} < \frac{\cos\alpha_n}{\cos\alpha_n + 1} < \frac{1}{1+1} = \frac{1}{2} \quad (2)$$

When this system is non-backdrivable ($\beta < \varphi$), its efficiency is by design less than 50%. Such efficiency is problematic as it requires dimensioning the motor to provide at least twice the torque compared to without this system.

Worm drives and screw-nut systems are still widely used in poly-articulated prostheses, where a motor and its transmission are needed for each finger. They have the advantage of being simple to design and well-mastered, as well as acting as a reduction stage.

2.3 Friction Disk System. The friction disk system described here is derived from the tridigital prosthesis *Myoelectric hand A+* by Danyang Reborn. It seems that no similar mechanism has been described in the scientific literature, which is why a preliminary analysis is proposed here.

The mechanism is shown in Fig. 1 in the blocking mode and the rotating mode in one direction of operation. It consists of an input shaft with two oblong pins, an output pinion, a ring fixed to the chassis, and a friction disk that rubs against the walls of the ring.

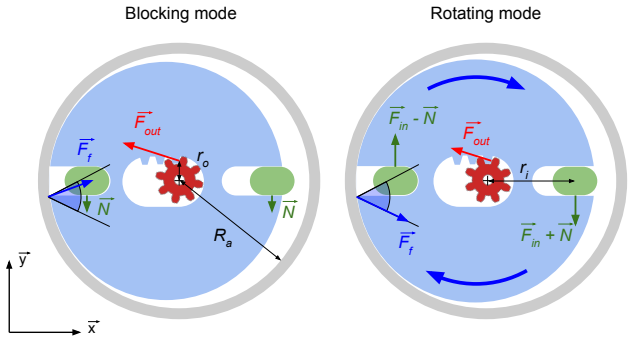

Fig. 1 Principle of the friction disk mechanism used in the tridigital prosthesis *Myoelectric hand A+* by Danyang Reborn, presented with forces acting on the friction disk in one direction of operation

In the blocking mode, an external torque is applied to the pinion, which, through teeth on the friction disk, presses it against the ring. The friction between the disk and the ring is sufficient to block the assembly from rotating. In the rotating mode, an input torque is applied via the two oblong pins. While the load continues to press the friction disk against the ring wall, the input torque allows overcoming the friction to rotate the assembly. However, friction causes energy losses.

To understand the interest of such a mechanism, it is necessary to analyze the conditions of its operation. Let α be the contact angle of the teeth between the pinion and the disk, μ the coefficient of friction between the disk and the ring, τ_{in} the torque on the input shaft, and τ_{out} the torque on the output shaft. The forces acting on friction disk are defined on Fig. 1 and $\vec{x}$ and $\vec{y}$ denote the unit

[2] Documentation available at https://gitlab.com/bionico/bionicohand

vectors of the plane. In the blocking mode, we can write:

$$\begin{cases} -(\vec{F}_{out}\cdot\vec{x})r_o - (\vec{F}_f\cdot\vec{y})R_a + (N\cdot\vec{y})r_i - (N\cdot\vec{y})r_i = 0 \\ (\vec{F}_{out}\cdot\vec{x}) + (\vec{F}_f\cdot\vec{x}) = 0 \\ \tau_{out} = -(\vec{F}_{out}\cdot\vec{x})r_o \end{cases} \tag{3}$$

The geometric condition that guarantees the non-backdrivability of the mechanism is found in the no-slip equation:

$$\begin{aligned} (\vec{F}_f\cdot\vec{y}) < \mu(\vec{F}_f\cdot\vec{x}) &\Leftrightarrow (\vec{F}_f\cdot\vec{y}) < -\mu(\vec{F}_{out}\cdot\vec{x}) \\ &\Leftrightarrow (\vec{F}_f\cdot\vec{y}) < \mu(\vec{F}_f\cdot\vec{y})\frac{R_a}{r_o} \\ &\Leftrightarrow \frac{r_o}{R_a} < \mu \end{aligned} \tag{4}$$

In the rotating mode, the force balance gives:

$$\begin{cases} -(\vec{F}_{out}\cdot\vec{x})r_o - (\vec{F}_f\cdot\vec{y})R_a - 2(\vec{F}_{in}\cdot\vec{y})r_i \ldots \\ \quad +(N\cdot\vec{y})r_i - (N\cdot\vec{y})r_i = 0 \\ (\vec{F}_{out}\cdot\vec{x}) + (\vec{F}_f\cdot\vec{x}) = 0 \\ (\vec{F}_f\cdot\vec{y}) = -\mu(\vec{F}_f\cdot\vec{x}) \\ \tau_{out} = -(\vec{F}_{out}\cdot\vec{x})r_o \\ \tau_{in} = 2(\vec{F}_{in}\cdot\vec{y})r_i \end{cases} \tag{5}$$

The efficiency can then be calculated:

$$\begin{aligned} \eta = \frac{\tau_{out}}{\tau_{in}} &= \frac{-(\vec{F}_{out}\cdot\vec{x})r_o}{2(\vec{F}_{in}\cdot\vec{y})r_i} = \frac{-(\vec{F}_{out}\cdot\vec{x})r_o}{-(\vec{F}_{out}\cdot\vec{x})r_o - (\vec{F}_f\cdot\vec{y})R_a} \\ &= \frac{(\vec{F}_f\cdot\vec{x})r_o}{(\vec{F}_f\cdot\vec{x})r_o + \mu(\vec{F}_f\cdot\vec{x})R_a} = \frac{r_o}{r_o+\mu R_a} = \frac{1}{1+\mu\frac{R_a}{r_o}} \end{aligned} \tag{6}$$

When the non-backdrivability condition is met, the term $\mu\frac{R_a}{r_o}$ is greater than 1, and the efficiency of the mechanism is then less than 50%. This mechanism presents the same efficiency issue as the worm drive.

2.4 Roller System. The main non-backdrivable mechanism proposed in the scientific literature comes from an Italian team that proposes a design approach to adapt freewheels with rollers into a non-backdrivable mechanism, in the context of a prosthetic finger [5].

The functioning of the mechanism is shown in Fig. 2. The output shaft has a cam geometry, which presses the rollers against the outer ring in the blocking mode. The assembly is blocked by the rollers adhering to the ring. The input shaft has a set of pins to release the rollers and another set of pins to drive the output cam. When the input shaft is driven in the rotating mode, the entire mechanism can rotate.

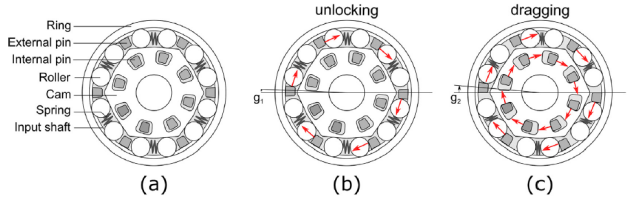

Fig. 2 Roller non-backdrivable mechanism at rest (a), during unlocking (b), and in the rotating mode (c) [5]

The reported performances of this mechanism allow achieving a maximum efficiency of 95% [4]. A major drawback of this type of mechanism is its complexity of implementation. A lot of fine pieces are required (rollers, springs), and the input and output shafts have complex geometries (cam, pins) that require tight manufacturing tolerances. Thus, the manufacturing cost is expected to be high due to the use of precision machining equipment. The authors also report wear effect on contact surfaces, which would need regular maintenance to keep the mechanism working as expected.

2.5 Wrap Spring System. The solution used by Ottobock is inspired by wrap spring freewheels. This solution does not seem to be described in the literature, although it has been used for several decades.

Wrap springs are often freewheeling between an input shaft and an output shaft. Here, the wrap spring is linked at both ends by two crowns A and B. The relative rotation between the two crowns blocks or unlocks the mechanism depending on the direction of this rotation. Specific geometries on the input and output shafts and on the crowns ensure the principle of non-backdrivability. When the input shaft is in contact with the crowns, the spring unlocks regardless of the rotation direction. Conversely, if the output shaft is driven while the input shaft is left free, the spring locks regardless of the direction. This non-backdrivable mechanism is shown in Fig. 3.

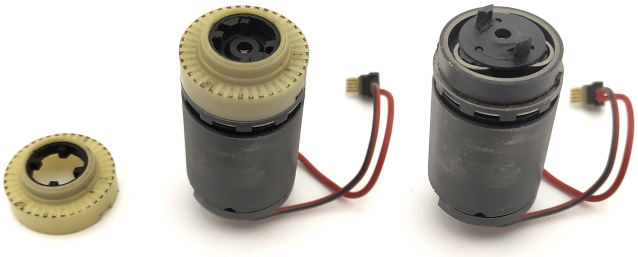

Fig. 3 Non-backdrivable mechanism used by Ottobock in the *VariPlus Speed*. On the left, the mechanism is shown alone; in the middle, the mechanism is mounted on the gearmotor; on the right, the gearmotor is shown alone. The wrap spring is placed between the black crowns and the yellow chassis and is not visible.

A solution based on the same operating principle is proposed later, and a more detailed analysis of the operation and efficiency of such a mechanism is available.

The system developed by Ottobock has an unmatched advantage of compactness. The diameter of the used spring wire is only a few tenths of a millimeter, and the function is performed within a cylindrical volume of 15 mm in diameter and 3 mm in height. Besides the spring, the rotating parts are made of plastic, which reduces the mass of the system and lowers the cost for large volumes.

Among the disadvantages of this mechanism is the high manufacturing cost for low volumes. Each plastic piece requires an injection mold, and the crowns must be over-molded or glued to the spring. Also, the crowns must be guided in rotation, so the materials used must be particularly suitable to limit friction. Finally, although no statistics allow for a proper evaluation of the robustness of this mechanism, we have found defects in some of these prostheses, probably related to the fragility of particularly thin pieces.

It should be remarked that the same principle of the non-backdrivable mechanism is used in the Ottobock *Greifer* myoelectric gripper, but its implementation is slightly different. In particular, a spring with a rectangular section is used, and this spring is blocked against an inner shaft instead of an outer crown.

3 Principle and Modeling of a Non-backdrivable Mechanism with Wrap Spring

3.1 Principle of the Non-backdrivable Mechanism. The proposed mechanism is an evolution of the wrap spring-based mechanism used by Ottobock in its tridigital prostheses, with the aim of reducing the number of parts and facilitating their fabrication.

Wrap springs are torsion springs, mainly used in freewheel applications. They have the particularity of being able to slide against a shaft or bore with little friction in one rotational direction but remain locked on the shaft or bore in the other direction, where the friction is much higher. They utilize the Capstan effect, which is defined as: Let flexible cable be wound around a cylinder. The ratio between the applied tension T_1 at one side of the flexible cable and the resulting tension T_2 at the other side of the flexible cable is given by

$$\frac{T_1}{T_2} = e^{\mu\phi}$$

Where μ is the coefficient of friction between the cable and the cylinder, and ϕ is the total angle swept by all turns of the cable. The capstan effect allows a significant amplification of friction to block the rotation of the spring.

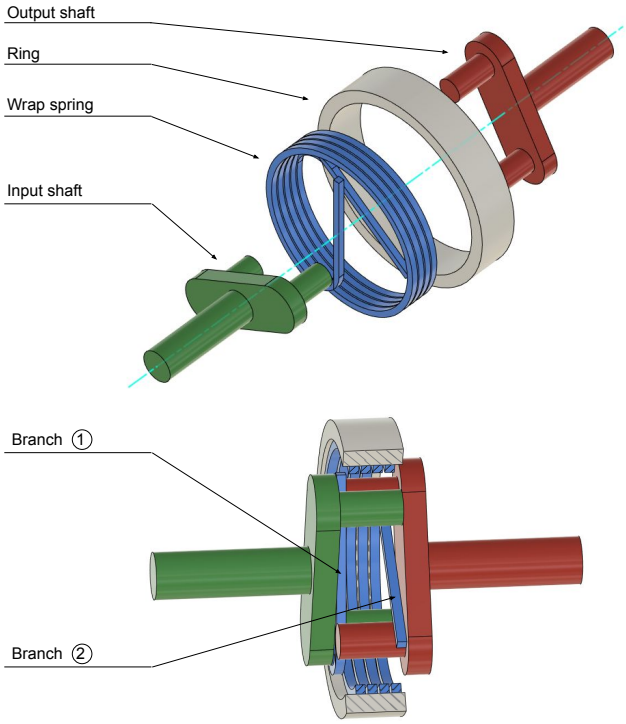

Fig. 4 Principle of the proposed mechanism, composed of three rotating parts (input shaft, output shaft, and spring) and the ring fixed to the chassis

The mechanism consists of four parts, as shown in Figure 4. An input shaft, linked to the motor's movement, has two offset pins. An output shaft, linked to the fingers of the prosthesis, is identical to the input shaft in its geometry. The wrap spring is a torsion spring whose legs are folded along the diameter of the spring. The two legs intersect to form an "X". Finally, a ring-shaped part linked to the chassis completes the assembly, having a bore that can accommodate the spring. All these parts are coaxial.

Figure 5 details the operating principle of the non-backdrivable mechanism. The input and output shafts are mounted so that their respective pins are on opposite sides of the "X" formed by the

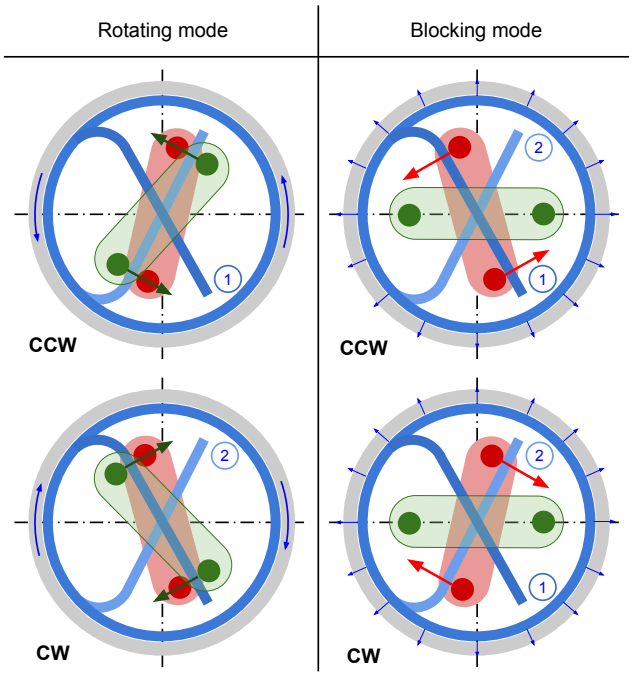

Fig. 5 Functioning of the mechanism according to the direction (CW=clockwise, CCW=counterclockwise) and origin of movement. When the input shaft is driven in motion, it, in turn, drives the spring and then the output shaft in rotation. When the output shaft is driven, it pushes the spring, which locks against the fixed ring, and the input shaft remains free.

spring's legs. Thus, these pins cannot be in direct contact. When the input shaft is driven by the motor, it comes into contact with one leg of the spring. In the counterclockwise direction, it presses on leg ②, and the spring is driven in its free direction. The spring then drives the output shaft, and the movement is transmitted. In the clockwise direction, the input shaft presses on leg ①, also driving the spring in its free direction. This is the rotating mode of the non-backdrivable mechanism. Conversely, when a torque is applied to the output shaft, it comes into contact with leg ① in the counterclockwise direction and with leg ② in the clockwise direction, always pushing on the spring in its blocking direction. The spring then presses against the fixed ring wall and sufficiently to lock and transmit torque to the chassis, preventing the transmission of torque to the input shaft. This is the blocking mode of the non-backdrivable mechanism.

While Ottobock mechanism necessitates two crowns attached to the spring to contact the input and output shaft, no intermediate part is used in the proposed solution. The absence of intermediate rotating parts mainly retrieves the complexity of their rotational guiding and limits both the number and complexity of manufactured parts.

3.2 Review of Wrap Springs. Here are the two main relationships that characterize the operation of the wrap spring [10,11], expressing the limiting slip torque τ^b in the blocking direction and the limiting slip torque τ^f in the free direction in terms of the spring's characteristics:

$$\tau^b = \frac{EI_z}{r_n^2}\delta r(e^{2\pi N_a \mu} - 1) \quad (7)$$

$$\tau^f = \frac{EI_z}{r_n^2}\delta r(1 - e^{-2\pi N_a \mu}) \approx \frac{EI_z}{r_n^2}\delta r, \quad \text{with } N_a\mu > 1 \quad (8)$$

where E and I_z respectively represent Young's modulus of the material and the moment of inertia related to the spring's section. The parameter r_n denotes the neutral radius or mean radius of the spring when no force is applied to it, and r_a is the mean radius of the spring when it is in its ring. The interference radius δr corresponds to the reduction in the spring's radius when it is mounted in the ring. We note N_a as the number of coils in contact with the ring and μ as the coefficient of friction between the spring and its ring. These equations are given under the assumption that the neutral radius r_n is much larger than the wire radius r_s of the spring. The mentioned parameters are presented in Figure 6.

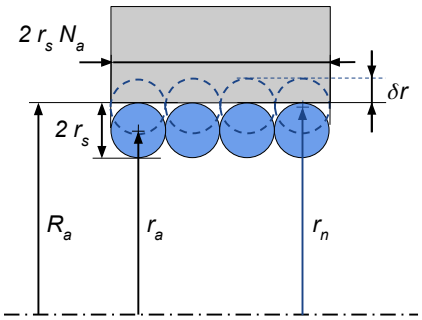

Fig. 6 Geometric parameters of the used wrap spring

The parameters in Figure 6 are related by the following two geometric relationships:

$$\delta r = r_n - r_a \tag{9}$$

$$R_a = r_a + r_s \tag{10}$$

3.3 Quantification of System Performance. For this system to function, it is imperative to have minimal friction between the spring and the fixed ring. This minimal friction is amplified by the Capstan effect in the blocking mode. It is therefore important to quantify the effect of this friction on the mechanism's performance.

We seek here to determine the efficiency of the mechanism in the rotating mode. The torque on the output shaft τ_{out} is expressed in terms of the friction torque τ^f (corresponding to the limiting slip torque in the free direction of the spring according to Eq. (8)), and the torque on the input shaft τ_{in}:

$$\tau_{out} = \tau_{in} - \tau^f \tag{11}$$

The input and output speeds are equal, and the efficiency η corresponds to the torque ratio between the output and input. Thus, we have:

$$\eta = \frac{\tau_{out}}{\tau_{in}} = \frac{\tau_{in} - \tau^f}{\tau_{in}} = 1 - \frac{1}{\tau_{in}} \frac{EI_z}{r_n^2} \delta r \tag{12}$$

The efficiency is zero when $\tau_{in} = \tau_f$ and increases with τ_{in}. We are mainly interested in the efficiency when τ_{in} is maximal, as this case determines the maximum clamping force of the prosthesis, and the Joule losses of the motor are particularly unfavorable for the highest torques.

We introduce K_b as the ratio between the maximum applicable torque on the output shaft τ_{out}^{max} and the maximum torque on the input shaft τ_{in}^{max} such that $\tau_{out}^{max} = K_b \tau_{in}^{max}$. K_b must be determined by the specifications: if we want to ensure the functioning of the non-backdrivable mechanism with a force on the fingers that is 20% higher than the maximum clamping force, then $K_b = 1.2$.

It is imperative that the limiting slip torque in the blocking direction of the spring τ_b is greater than or equal to τ_{out}^{max} to ensure that the prosthesis does not loosen when the motor torque is released. In an initial pre-dimensioning phase, we consider $\tau_b = \tau_{out}^{max}$, and we fix K_b to a chosen value. We can write the following relation:

$$\begin{aligned} \eta_{max} &= \frac{\tau_{in}^{max} - \tau^f}{\tau_{in}^{max}} = \frac{\tau^b/K_b - \tau^f}{\tau^b/K_b} = 1 - K_b \frac{\tau^f}{\tau^b} \\ &= 1 - \frac{K_b}{e^{2\pi N_a \mu} - 1} \end{aligned} \tag{13}$$

We deduce that for a given K_b, increasing the number of coils and the coefficient of friction allows an exponential increase in efficiency. Taking $K_b = 1.5$, we need $N_a\mu = 0.55$ to obtain $\eta_{max} = 95.0\%$ or $N_a\mu = 0.8$ to obtain $\eta_{max} = 99.0\%$. Therefore, very good efficiencies are possible.

3.4 Modeling of Stress in the Spring. Before establishing a sizing procedure, we are interested in the mechanical limits of the mechanism. The limiting factor is the resistance of the spring's branch to bending stresses, under the maximum applied torque τ_{out}^{max}.

3.4.1 Parameterization of the Spring Branch. The different geometric parameters that define the geometry of the spring branch are presented in Figure 7. To simplify the problem, we consider that the bend radius R is much smaller than the spring radius R_a, and that the fixation is parallel to the spring branch. Therefore, the spring bend is modeled as a quarter of a circle.

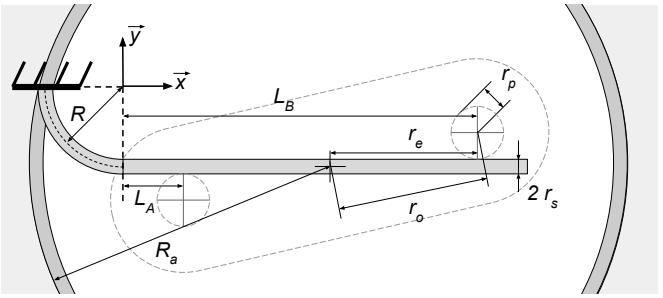

Fig. 7 Geometric parameterization of the modeled spring branch as a simply supported beam

The branch is described by the parameters R, L_A, L_B, R_a, r_e, and r_s, as well as the following two relations:

$$L_B - L_A = 2r_e \tag{14}$$

$$R_a = \sqrt{R^2 + (R + r_s + L_A + r_e)^2} \tag{15}$$

The branch is fully determined once R_a, R, r_s, and r_e are fixed. The input and output shafts are determined by the parameters r_o and r_p, and they are related to the branch's geometry by the following relation:

$$r_o = \sqrt{r_e^2 + (r_p + r_s)^2} \tag{16}$$

The forces applied to the spring branch are shown in Figure 8. The moment balance on the output shaft gives:

$$(F_A - F_B) r_e = \tau_{out}^{max} \tag{17}$$

Since the problem is statically indeterminate, it is not possible to determine the forces F_A and F_B with a single force balance. However, knowledge of these forces is necessary to evaluate the stress in the branch.

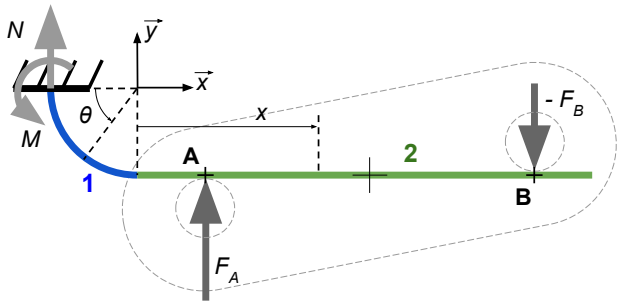

Fig. 8 Modeling of the simply supported beam subjected to two forces, composed of a first section formed by a quarter of a circle denoted as 1, and a second straight section denoted as 2

3.4.2 Determination of forces through deformation calculation. To provide information about this hyperstatic problem, the study of displacements is of interest. We observe that the two pins of the shaft are constrained to move together. In particular, we know that the displacement δ_A of point **A** is opposite and equal in magnitude to the displacement δ_B of point **B**, so that the center of segment AB remains fixed. Therefore, we have the relationship $\delta_A = -\delta_B$, where δ_A and δ_B are counted positively along the $\vec{y}$ axis.

By using Castigliano's theorem, it is possible to relate the displacements δ_A and δ_B to the forces F_A and F_B. The forces F_A and F_B can then be determined based on the geometric data of the branch L_A, L_B, and R, as well as the maximum torque τ_{out}^{max} and the lever arm r_e.

Eq. (18) Castigliano's theorem can be written in its general form [12] where U_{1+2} is the strain energy in the sections 2 and 3. For a beam subjected to bending, the strain energy is expressed in eq. (19) with $Mf_z(\theta)$ and $Mf_z(x)$ the bending moment around $\vec{z}$ axis respectively in sections 2 and 3, θ and x the coordinates respectively in sections 2 and 3 where moment is applied, E the Young modulus of the spring material, I_z the moment of inertia of the spring around $\vec{z}$ axis [12].

$$\delta_A = \frac{\partial U_{1+2}}{\partial F_A} \quad , \quad \delta_B = \frac{\partial U_{1+2}}{\partial F_B} \tag{18}$$

$$U_{1+2} = U_1 + U_2 = \frac{1}{2}\int_0^{\pi/2} \frac{Mf_z^2(\theta)}{EI_z} R\mathrm{d}\theta + \frac{1}{2}\int_0^{L_B} \frac{Mf_z^2(x)}{EI_z}\mathrm{d}x \tag{19}$$

We finally obtain an expression of the following form, where f_A and f_B are functions of the geometrical parameters of the branch:

$$\begin{aligned} F_A &= f_A(L_A, L_B, R)\frac{\tau_{out}^{max}}{r_e} \\ F_B &= -f_B(L_A, L_B, R)\frac{\tau_{out}^{max}}{r_e} \end{aligned} \tag{20}$$

Next, we can calculate the forces at the fixation point:

$$\begin{aligned} N &= -F_A - F_B \\ M &= -F_A(L_A + R) - F_B(L_B + R) \end{aligned} \tag{21}$$

3.4.3 Stress Calculation. The maximum stresses in the spring branch can be determined from the previously calculated forces.

The maximum stresses occur where the bending moment is maximal, either in one direction or the other. Mf_z reaches its extreme values at the fixation point and at point **A**. It is therefore necessary to evaluate the stresses at these two points.

At the fixation point, we use the theory of curved beams to evaluate the stress σ [13] :

$$\sigma = \sigma_{normal} + \sigma_{flexion} = \frac{N}{A} + \frac{My}{Ae(R - e - y)} \tag{22}$$

where A is the area of the considered section, e is the distance between the centroid and the neutral axis, and y is the distance between the point where the stress σ is evaluated and the neutral axis.

The stress can be maximum on the inner fiber (σ_{int}) or the outer fiber (σ_{ext}). From equation (22), we obtain:

$$\sigma_{int} = \frac{N}{A} + \frac{M(r_s - e)}{Ae(R - r_s)} \quad , \quad \sigma_{ext} = \frac{N}{A} - \frac{M(r_s + e)}{Ae(R - r_s - 2e)} \tag{23}$$

For a square section, the parameters e and A are given by the following expressions [13] :

$$e = R - \frac{2r_s}{\ln(\frac{R+r_s}{R-r_s})} \quad , \quad A = 4r_s^2 \tag{24}$$

For a circular section, the parameters e and A are given by the following expressions [13] :

$$e = R - \frac{4r_s^2}{8\left(R - \sqrt{R^2 - r_s^2}\right)} \quad , \quad A = \pi r_s^2 \tag{25}$$

At point **A**, the equivalent von Mises stress σ_A is expressed as follows :

$$\begin{aligned} \sigma_A &= \sqrt{\sigma_{flexion}^2 + 3\sigma_{shear}^2} \\ &= \sqrt{\left(\frac{Mf_z r_s}{I_z}\right)^2 + 3\left(\frac{T}{A}\right)^2} \\ &= \sqrt{\left(\frac{2F_B r_e r_s}{I_z}\right)^2 + 3\left(\frac{F_A - F_B}{A}\right)^2} \end{aligned} \tag{26}$$

The most significant stress will be critical for the system, denoted as:

$$\sigma_{max} = \max(|\sigma_{int}|, |\sigma_{ext}|, |\sigma_A|) \tag{27}$$

3.5 Modeling of Backlash and Geometry at Rest. The proposed non-backdrivable mechanism is not free of backlash. The backlash at the output shaft β_o requires special attention as it will affect the fingers' behavior. It is also noted that the angle between the branches is different when the spring is in the ring compared to when the spring is under no load before the assembly. It is essential to determine the relationship between these angles to ensure obtaining the desired angles and backlash once the device is assembled. Figure 9 shows the definition of the various angles that characterize the backlash and the geometry at rest.

The relationships between the different angles and lengths when the spring is assembled are as follows:

$$\alpha_o = \beta_o + 2\arcsin\left(\frac{r_p}{r_o}\right) + 2\arctan\left(\frac{r_s}{r_e}\right) \tag{28}$$

$$\varphi_a = \alpha_i - 2\arcsin\left(\frac{R}{r_a - R}\right) \tag{29}$$

N_a is determined up to the nearest turn to respect the "X" geometry of the branches.

$$N_a = k + \frac{\varphi_a}{2\pi} \qquad \text{where } k \in \mathbb{N} \tag{30}$$

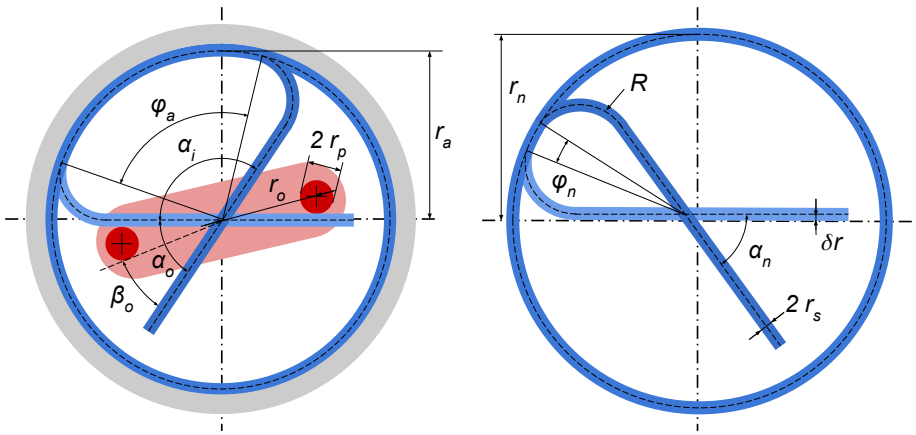

Fig. 9 Definition of angles when the spring is in the ring and when the spring is at rest before the assembly

The corresponding relationships describe the spring at rest:

$$\varphi_n = \alpha_n - 2\arcsin\left(\frac{R}{r_a - R}\right) \tag{31}$$

$$N_n = k + \frac{\varphi_n}{2\pi} \qquad \text{where } k \in \mathbb{N} \tag{32}$$

Finally, the conservation of the spring wire length allows expressing the relation between the number of coils at rest and the number of active coils when mounted:

$$2\pi N_n r_n = 2\pi N_a r_a \Leftrightarrow N_n = N_a \frac{r_a}{r_n} \Leftrightarrow N_n = N_a \frac{R_A - r_s}{R_A + \delta r} \tag{33}$$

4 Mechanism Design Procedure

The results presented above are calculated for a square section, but the observations are identical for a circular section. Only the presented values would change.

4.1 Formulation of Design Objectives. Figure 6 presents six parameters, and the two relationships (9) and (10) reduce the number of independent parameters to four to define the spring profile. Figure 7 provides six parameters to define the geometry of the spring branches and two parameters to define the geometry of the input and output shafts. Two relationships (14) and (15) reduce the number of independent parameters to four for the spring branches, and the relationship (16) limits the number of independent parameters to one for the input and output shafts.

Overall, nine independent geometric parameters completely describe the functioning of the mechanism, to which the friction coefficient μ depending on the materials used and the shape of the spring section, square or circular, is added.

The set of parameters used must meet the following objectives and constraints:

- When the input shaft is driven, the torque must be transmitted to the output shaft with the highest possible efficiency, with an objective of 95% and an acceptable lower limit of 85%.
- When the input shaft is released, the load torque on the output shaft must not cause the entire mechanism to rotate.
- The radial size must be limited to a selected value to allow for the integration of the mechanism with a limit set to 25mm of diameter for this work.
- The axial size should be as small as possible with a limit set to 20mm of length for this work.
- The spring must not undergo plastic deformation over its entire operating range.
- The spring must be manufacturable using conventional industrial tools and "reasonable" tolerances, meaning it can be produced at a low cost by most spring manufacturers.

4.2 Design of Slipping Torques. By combining Eqs. (7) and (8), we can write:

$$\tau^b \approx \tau^f (e^{-2\pi N_a \mu} - 1) \tag{34}$$

To maximize the efficiency in the rotating mode, it is necessary to minimize τ^f as much as possible. However, it is imperative to keep τ^b higher than τ_{out}^{max} to ensure blocking in the blocking mode. The strategy is therefore to minimize τ^f and increase the term $N_a\mu$ accordingly.

4.2.1 Minimization of Friction Torque in the Rotating Mode. To minimize τ^f, it is useful to analyze the impact of the different defining terms. We choose to fix the terms R_a, corresponding to the radial size of the mechanism, r_s corresponding to the selected spring wire size, and δr for the radial interference.

$$\tau^f = \frac{EI_z}{r_n^2}\delta r \propto \frac{r_s^4}{(R_a - r_s + \delta r)^2}\delta r \approx \frac{r_s^4}{R_a^2}\delta r \tag{35}$$

with $(\delta r - r_s) \ll R_a$.

This relationship shows that firstly, R_a must be maximized, while r_s and δr must be minimized. Each term is bounded as follows:

- R_a is set to its maximum "acceptable" radial size to allow for integration into the prosthesis.
- r_s is set to its minimum value that ensures the mechanical strength of the system. This value is determined in section 4.3.
- δr is set based on the manufacturing tolerances on the diameter of the ring and the spring. If the effective δr obtained after fabrication is too small, the resulting τ^b torque may be too low. To properly control the slipping torques, it is proposed to have $\delta r > 4I^T$, where I^T is the tolerance interval on the radius.

Figure 10 presents the variation of τ^f as a function of r_s and δr for a fixed radius R_a. It can be observed that minimizing r_s and δr allows minimizing τ^f effectively.

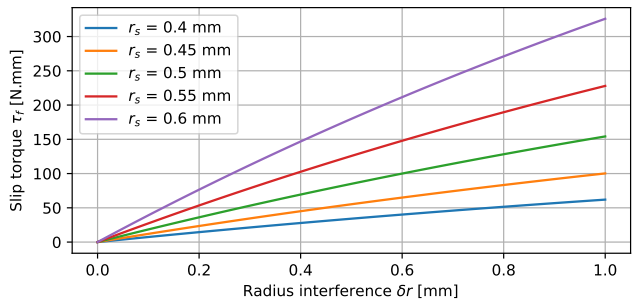

Fig. 10 Friction torque in the rotating mode τ^f as a function of δr and r_s for R_a =10 mm

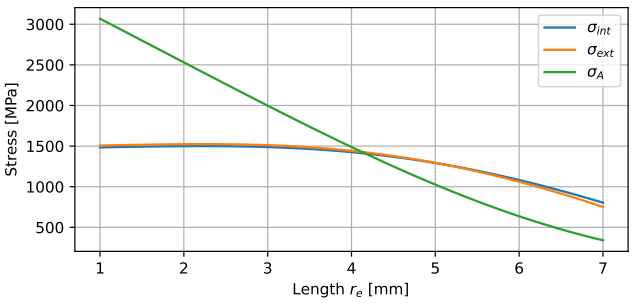

Fig. 11 Stresses σ_{int}, σ_{ext}, and σ_A as a function of r_e for τ_{out}^{max} = 600 N.mm, R_a = 10 mm, R = 3 mm, and r_s = 0.5 mm

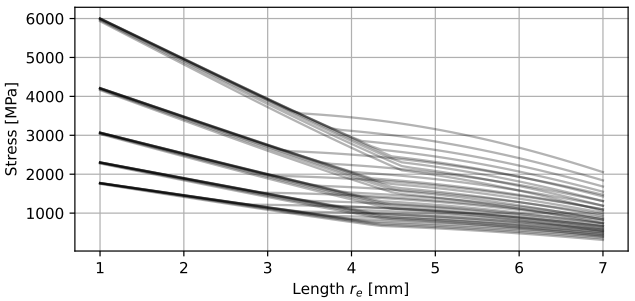

Fig. 12 Set of curves presenting the maximum stress σ_{max} as a function of r_e, plotted for τ_{out}^{max} = 600 N.mm, R_a = 10 mm, and all pairs (R; r_s) such that R ∈{1.5, 2, 2.5, 3, 3.5, 4, 4.5, 5.0} mm and r_s ∈{0.4, 0.45, 0.5, 0.55, 0.6} mm

4.2.2 Determination of the Blocking Torque. Once the parameters R_a, r_s, and δr have been fixed, the parameters N_a and μ need to be determined.

Firstly, the friction coefficient μ depends on the material pair selected for the spring and the fixed ring. A common and robust material for spring manufacturing is stainless steel 302 (according to the EN 10270-3 standard). The material for the ring is selected based on several criteria. For instance, one may decide to use a specific ring or directly use the body of the prosthesis chassis and maintain the same material. A material pair with a high friction coefficient like the Steel-Aluminum pair can be advantageous in limiting the number of required turns N_a. However, the ring will likely wear out faster than with a Steel-Bronze pair having a lower friction coefficient. Lubrication also plays a role in determining the value of μ and the long-term wear. In this study, wear-related issues are set aside.

Once μ is fixed, we calculate the smallest possible N_a to satisfy the following condition:

$$\tau^b > \tau_{out}^{max} \Leftrightarrow \frac{EI_z}{r_n^2}\delta r(\mathrm{e}^{2\pi N_a \mu} - 1) > \tau_{out}^{max}$$

$$\Leftrightarrow N_a > \frac{1}{2\pi\mu}\ln(\tau_{out}^{max}\frac{r_n^2}{EI_z\delta r} + 1) \quad (36)$$

We remind that N_a is determined to the nearest integer to respect the geometry of the branches, according to Eq. (30).

4.3 Branches Design. The geometry of the branch is defined by four independent parameters, as previously shown from figure 7.

4.3.1 Determination of the Lever Arm r_e. We start by evaluating the impact of r_e on the stresses in the branch. Figure 11 presents the stresses as a function of r_e. The stress is maximum at point A when r_e is small, and at the base of the branch when r_e increases. It can be observed that these stresses strictly decrease as a function of r_e.

It is possible to verify this decrease for several values of elbow radius R and wire radius r_s. Figure 12 shows the evolution of the maximum stress as a function of r_e for a large number of parameter sets (R, r_s). It can be observed that the stress always decreases with increasing r_e.

Therefore, the value of r_e is logically fixed at its maximum value. This value is constrained by the location of point A, which should not be within the arc of the circle, meaning $L_A \geq 0$. To be robust to manufacturing imperfections, we set L_A = 0.5 mm, and r_e is then determined from the expression (15).

4.3.2 Determination of the Bend Radius R. Next, it is observed that the variation of R has a dual effect. On one hand, increasing R reduces stress concentrations inside the bend. On the other hand, this increase also leads to a decrease in r_e maximal value, increasing the stresses as explained previously.

Figure 13 shows the evolution of the maximum stress as a function of R for several values of r_s. The stress σ_{max} increases as R increases or as r_s decreases. Thus, R is fixed at the minimum possible radius during spring fabrication.

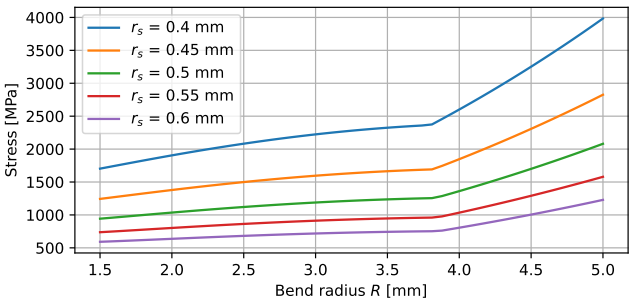

Fig. 13 Stress σ_{max} as a function of R and r_s for τ_{out}^{max} = 600 N.mm, R_a = 10 mm, and L_A = 0.5 mm

4.3.3 Determination of the Wire Radius r_s. Finally, the wire radius r_s is determined by selecting the smallest value that ensures σ_{max} remains below a specified threshold. In practice, it is customary to define a safety factor s and verify that $\sigma_{max} < sR_e$, where R_e is the material's yield strength.

Firstly, it should be noted that the material's yield strength is dependent on the wire radius r_s, which in turn depends on the spring wire manufacturing process. Additionally, the choice of r_s is limited to a list of available wire diameters, and not all values

are possible. Manufacturers offer wire diameters in increments of 0.1 mm, resulting in r_s values that are multiples of 0.05 mm.

Figure 14 allows visualization of the maximum stress and the yield strength as a function of r_s. In the given example, choosing a wire radius of $r_s = 0.45$ mm ensures compliance with the yield strength with a safety factor $s = 1.2$.

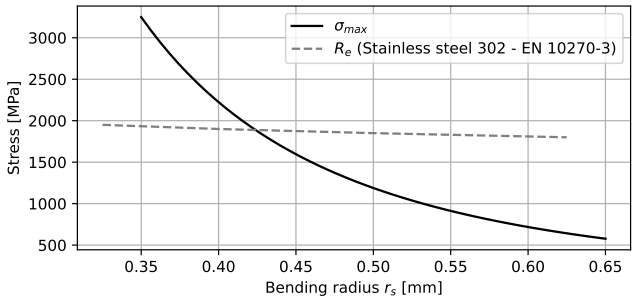

Fig. 14 Stress σ_{max} as a function of r_s for $\tau_{out}^{max} = 600$ N.mm, $R = 3$ mm, $R_a = 10$ mm, and $L_A = 0.5$ mm, compared to the material's yield strength R_e provided by a manufacturer

4.4 Calculation of Geometry at Rest. The output backlash β_o is set by the designer. This backlash must be minimized while remaining strictly positive. Therefore, it is necessary to know the manufacturing tolerances for this type of shape to ensure the assembly of the system without significantly increasing the backlash.

Next, Eqs. (28), (29), and (33) allow determining all the construction angles.

4.5 Numerical Application. The application of the sizing procedure yields the numerical results presented in Table 1 for a nominal configuration. For each parameter, the criterion determining its value is indicated.

It is noted that δr has been intentionally chosen to be high to anticipate fabrication imperfections, and reducing its value would improve the system's efficiency.

4.6 Scaling and Torque Density. The proposed system has been sized for given maximum torques τ_{in}^{max} and τ_{out}^{max}. Firstly, it is interesting to evaluate the possibility of placing the non-backdrivable mechanism at a different level in the transmission. If placed closer to the motor or further upstream in the reduction, the torques would be lower, and its size would likely be smaller. If placed closer to the fingers or further downstream, the torques would be higher, and its size would be larger. Secondly, this mechanism could be used more broadly for other systems where the non-backdrivability is advantageous.

The goal is to determine how much the dimensions of the mechanism should be multiplied to adapt to torques multiplied by a factor K_τ. To achieve this, all dimensions of the system are multiplied by a factor K_D, and the multiplier K_τ for the torques is determined to maintain an equivalent maximum stress σ_{max} to its initial value. Table 2 provides several obtained values:

We observe a cubic relationship between K_D and K_τ. In other words, to keep the maximum stress constant, the volume of the mechanism must remain proportional to the imposed maximum torques. This relationship can be explained by analyzing Eq. (22), where the stress is calculated by dividing a moment in N.mm, proportional to τ_{out}^{max}, by a factor depending on the dimensions of the mechanism and expressed in mm^3.

We can then characterize the torque density D_τ of this non-backdrivable as the ratio between the maximum input torque τ_{in}^{max} and the volume V of the cylinder circumscribed around the spring.

$$D_\tau = \frac{\tau_{in}^{max}}{V} = \frac{\tau_{in}^{max}}{2\pi R_a^2 N_a r_s} \tag{37}$$

For the numerical application with a square section, we have $D_\tau = 0.8$ N.mm/mm^3. These values can also be used to compare with other available systems.

5 Experiments

5.1 Validation of Stress Model through Finite Element Simulation. The experimental measurement of stress in the spring to validate the proposed stress model in Section 4.3 is challenging to implement. Instead, a comparison is made with a finite element simulation before fabricating an experimental prototype. Since the geometry is simple, finite element simulation software (e.g., Fusion360) is considered reliable.

The branch is simulated by applying the forces F_A and F_B calculated using Eq. (20). Figure 15 shows the finite element simulation results. The maximum stress of 1,575 MPa is observed inside the bend (with an error of 1.3%). The maximum stress over the entire branch is 1,616 MPa, which is obtained at a single node on the edge where the force F_A is applied, suggesting a numerical singularity.

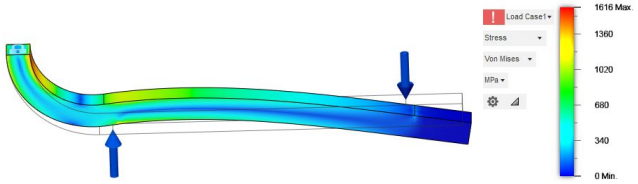

Fig. 15 Von Mises equivalent stress [MPa] obtained through finite element simulation of the spring branch in Fusion360 (deformation not to scale)

The simulation also verifies that the geometric condition $\delta_A = -\delta_B$ is met with the calculated forces F_A and F_B. The simulation yields $\delta_A = 0.101$ mm and $\delta_B = -0.108$ mm, with low error, confirming the validity of the proposed effort modeling.

5.2 Development of a Functional Prototype. A first functional prototype was designed as a proof of concept to validate the practical feasibility and the theoretical model proposed in this paper. The functional parts (spring and ring) of the prototype were designed to scale for future integration into a prosthesis and are comprised in a cylinder with a diameter of 25mm and a length of 13.2mm. The rest of the prototype was designed to facilitate fabrication and assembly leading to a chassis with a diameter of 45mm and a length of 42,7mm. The ring and the spring can be changed to allow experiments with various sets of parameters and different materials. The prototype is symmetrical, and the difference between the input shaft and output shaft occurs during assembly, depending on the placement of the pins between the spring branches. A cross-sectional view of the CAD and a photo of the prototype are presented in Figures 16 and 17, respectively.

To characterize the impact of varying several parameters around the nominal values proposed in Section 4.5, multiple springs and rings were fabricated. This allows changing the spring section, number of turns, ring material, and diameter.

5.3 Manufacturing Variability. Reducing the interference radius δr is critical for improving the mechanism's efficiency, and it should remain significantly larger than the manufacturing tolerance on the radius to ensure sufficient blocking mode torque. Four spring configurations, with two different sections and two different numbers of turns, were ordered from a manufacturer, each in three samples. The measurement results are presented in Table 3.

Parameters	Selected Values	Selection Criterion
τ_{in}^{max}	500 N.mm	Specifications
τ_{out}^{max}	600 N.mm	Specifications
R_a	10 mm	Maximized, limited by spatial constraints
δr	0.4 mm	Minimized, limited by fabrication precision
L_A	0.5 mm	Minimized, limited by fabrication precision
R	3 mm	Minimized, limited by manufacturing capabilities
r_s	0.45 mm	Minimized, limited by maximum stress
r_e	5.59 mm	Derived
L_B	11.68 mm	Derived
σ_{max}	1,595 MPa	Derived
r_p	2.0 mm	Sufficiently rigid pin
r_o	2.0 mm	Derived
β_o	10°	Minimized, limited by fabrication precision
α_o	39.2°	Derived
φ_a	86.3°	Derived
Ring Material	Steel	Hard material
Spring Material	Stainless Steel 302	Common and robust material
μ	0.2	Steel-steel pair
N_a	2.24	Steel-steel pair
τ^f	45 N.mm	Derived
τ^b	707 N.mm	Derived
η_{max}	91%	Derived
N_n	2.15	Derived
$alpha_n$	108.4°	Derived

Table 1 Numerical application of the procedure in the nominal configuration

K_D	K_τ	σ_{max} [MPa]
0.5	0.125	1,595
1	1	1,595
2	8	1,595
3	27	1,595
4	64	1,595

Table 2 Dimension multipliers K_D and torque multipliers K_τ to obtain a constant σ_{max} stress

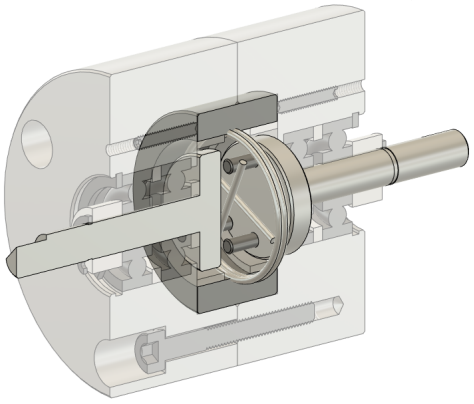

Fig. 16 Cross-sectional view of the non-backdrivable prototype (CAD)

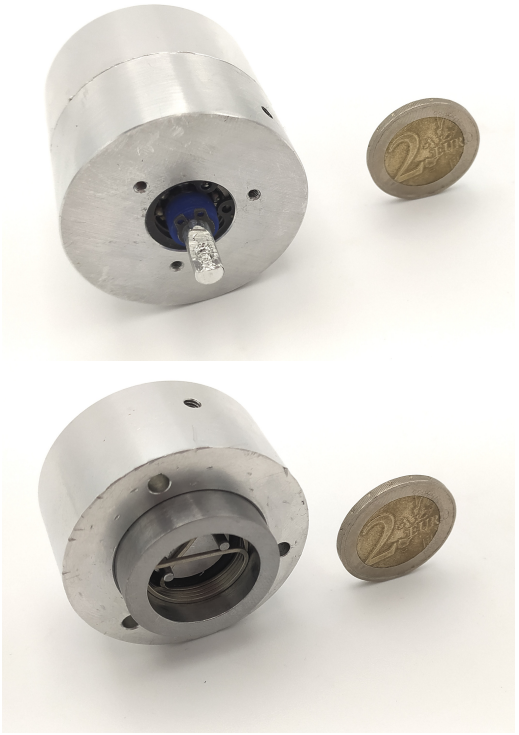

Fig. 17 Photo of the non-backdrivable prototype, fully assembled on the top, and partially assembled on the bottom

The measured variability in the outer diameter ranges from −0.07mm to 0.14mm, resulting in a variability of the interference radius δr from -7.0% to +17.5% compared to the nominal value. It is observed that the variability is more significant for square sections than for circular sections, consistent with the manufacturer's statements. It is also noted that the variations are not centered, and for larger production runs, calibrating the manufacturing machine could improve the average measurement.

5.4 Experimental Setup. An experimental test bench was developed to measure the friction torque τ^f in the rotating mode, to validate the proposed friction model according to the non-backdrivable mechanism parameters. The test bench is shown in Figure 18. It consists of a speed-controlled motor that rotates the input shaft of the non-backdrivable mechanism. The motor is attached to the bench's frame through a sliding pivot connection

Section	Theoretical N_n	Sample Number	ϕ Measured - ϕ Theoretical [mm]	Variation of δr
Square	2.15	1	0.03	+3.8%
Square	2.15	2	-0.03	-3.8%
Square	2.15	3	0.14	+17.5%
Square	3.11	1	0.10	+12.5%
Square	3.11	2	0.11	+13.8%
Square	3.11	3	0.09	+11.3%
Circular	2.13	1	-0.06	-6.0%
Circular	2.13	2	0.00	0.0%
Circular	2.13	3	-0.07	-7.0%
Circular	3.08	1	0.00	0.0%
Circular	3.08	2	-0.02	-2.0%
Circular	3.08	3	0.00	0.0%

Table 3 Variability of the outer diameter of springs during manufacturing for various characteristics

along its rotation axis and is held in rotation by a static torque sensor fixed to the frame to measure the torque produced by the motor. The output shaft of the non-backdrivable mechanism is linked to a dynamic torque sensor, which measures the output torque of the mechanism. Finally, the dynamic torque sensor is attached to an output load that allows varying the torque transmitted by the non-backdrivable mechanism. An adjustable brake is used to vary the load. The different elements are connected with elastic couplings that help reduce the impact of alignment errors on measurements.

The friction torque is determined by calculating the difference between the torque on the input shaft, τ_{in}^{mes}, provided by the static torque sensor, and the torque on the output shaft, τ_{out}^{mes}, provided by the dynamic torque sensor.

5.5 Friction Torque Measurements.

5.5.1 Conducted Experiments. The initial experiments aim to compare the theoretical friction values with the measured friction values. For this purpose, measurements are performed in the nominal configuration and also by varying the ring radius R_a, thereby reducing the interference radius δr and the friction torque in the rotating mode. Other parameters that are not expected to influence the friction torque, such as the material and the friction coefficient μ, the spring section, the number of active turns N_a, the rotational speed, and the output load τ_{out}, are also studied.

From the raw data obtained from the torque sensors (shown in Figure 19), several operations are conducted. Firstly, a calibration is performed to convert voltage measurements into torque signals. Next, the signals are filtered to reduce high-frequency noise. Finally, it is necessary to resample both signals on a common timestamp using interpolation methods since their initial acquisition is not synchronized. Subsequently, the friction torque can be calculated by obtaining the difference between the two signals.

5.5.2 Nominal Case and Interference Variation. Initially, the non-backdrivable mechanism is assembled in its nominal configuration (see sec. 4.5), and the measured torques are presented in Figure 19. An average friction torque $\overline{\tau^f}$ of 54.4 N.mm is recorded, compared to a theoretical torque of 45 N.mm, resulting in a deviation of 21%.

Although this difference is not negligible, it remains within an acceptable range for the operation of the non-backdrivable mechanism. The maximum efficiency of the non-backdrivable mechanism would then decrease from 91% to 89%.

5.5.3 Influence of the Load. The variation of the torque transmitted by the non-backdrivable mechanism does not theoretically impact the friction torque of the spring against the fixed ring. This behavior can be verified by varying the torque on the adjustable brake.

Figure 20 illustrates the evolution of τ_{in}, τ_{out}, and τ^f as the load imposed on the brake varies. It can be observed that the variations in torques τ_{in} and τ_{out} are similar, and the difference τ^f between these torques remains constant. The load does not influence friction in this mechanism.

5.5.4 Influence of the Rotational Speed. The variation of the rotational speed of the input and output shafts of the non-backdrivable mechanism also does not have an impact on the friction torque, according to the proposed theoretical model. However, there may be the presence of viscous friction (speed-dependent) that adds to dry friction, although it is not modeled. It is essential to verify that this viscous friction remains low compared to dry friction to avoid unexpected performance degradation. Here, the average friction $\overline{\tau^f}$ of the non-backdrivable mechanism is measured at different speeds.

Table 4 shows the different measurements obtained at different rotational speeds. There is a variation of up to 4% between the different experiments, but this variation appears to be random and not linearly correlated to the speed. It seems that these variations are related to experimental device inaccuracies, and the rotational speed does not have a measurable impact on the friction.

Speed [rad/s]	3	5	10	15	20	25
$\overline{\tau^f}$ [N.mm]	53.1	54.4	52.7	52.8	53.0	54.9

Table 4 Average friction torque of the non-backdrivable mechanism at different rotational speeds in the nominal configuration

5.5.5 Impact of Material. Three different materials for the ring are used: steel, aluminum, and bronze. For each material, the average friction torque is measured at various rotational speeds, and the experimental results are averaged. The obtained mean values of $\overline{\tau^f}$ are 54.5 N.mm for the steel ring, 90.4 N.mm for the bronze ring, and 126.0 N.mm for the aluminum ring. These differences are significant and indicate that the proposed model is inadequate for using bronze or aluminum.

However, these results do not necessarily imply that the impact of the friction coefficient is more significant than expected. The steel-aluminum combination has the highest friction coefficient and yields the highest friction torque, but the steel-bronze combination has the lowest friction coefficient and still produces a higher friction torque than the steel-steel combination.

Two main hypotheses are considered to explain this discrepancy between the model and the experimental results. Firstly, the surface roughness may play a role in causing friction much greater than expected. The surface roughness was not specified during manufacturing and was not measured. Secondly, the material hardness

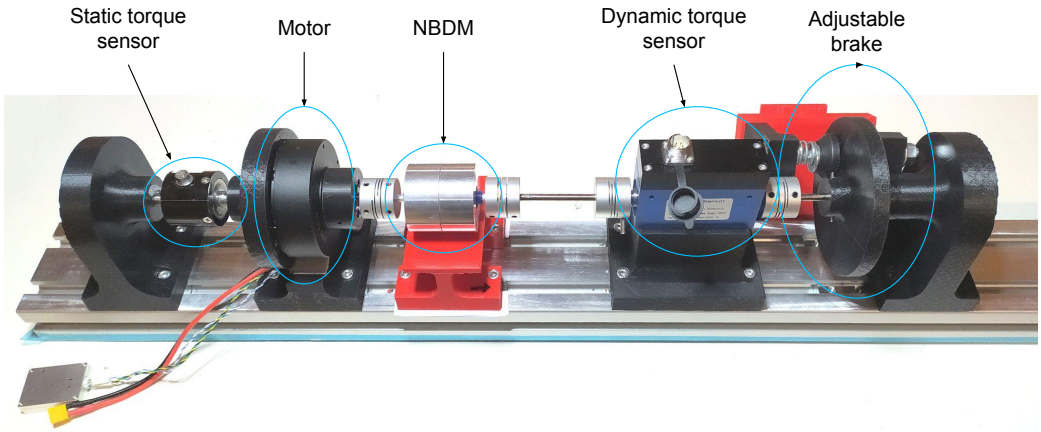

Fig. 18 Test bench for measuring friction torque in rotating mode

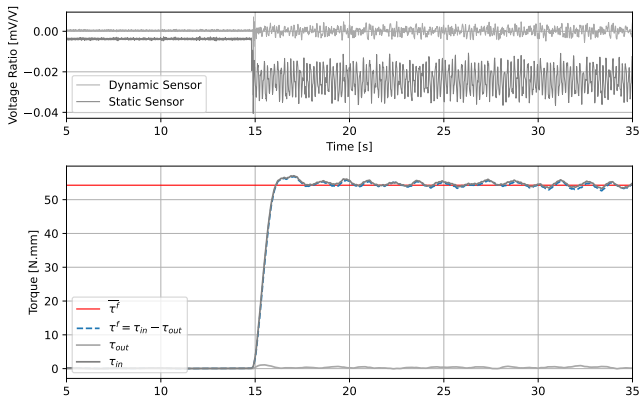

Fig. 19 Measurement of static and dynamic torque sensors and calculation of filtered torques in the nominal configuration with zero output load and a rotational speed of 5 rad/s

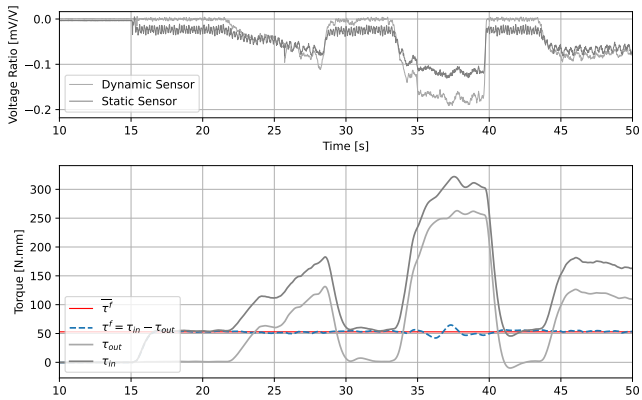

Fig. 20 Measurement of static and dynamic torque sensors and calculation of filtered torques in the nominal configuration with a variable output load and a rotational speed of 5 rad/s

may account for the differences observed. Indeed, steel is the hardest material, aluminum is the least hard, and bronze falls between the two. It should be noted that the surface of softer materials can deteriorate more quickly, leading to an increase in roughness over time during use.

5.6 Blocking Torque Measurements. To measure the blocking torque, the dynamic torque sensor, and the adjustable brake are not used. The non-backdrivable mechanism is mounted in the opposite direction so that the blocking side is fixed to the motor shaft. A speed setpoint is given to the motor, which adjusts its torque to exceed the blocking torque limit and cause the rotation of the non-backdrivable mechanism. The torque is measured between the chassis and the motor by the static torque sensor.

Several tests are conducted with the mechanism for the nominal configuration, and by using a spring with an additional active coil. The values are presented in Table 5. It can be observed that the measurements taken are highly variable for the same configuration.

Although these measurements exhibit high variability, some trends can be observed. Firstly, it is noticed that the measurements are much lower than those expected for a coefficient of friction $\mu = 0.2$. However, the measurements are of the same order of magnitude as the blocking torque for $\mu = 0.15$. This coefficient of friction is considered plausible in the case of steel-steel friction.

It was not possible to perform further measurements with this setup, as some tests resulted in irreversible deformation of the spring.

5.7 Improvement Perspectives. In order to consolidate the obtained results, improvements could be made to the mechanism and the test bench.

Firstly, the geometry of the branches exhibits significant manufacturing variability, and controlling this geometry is crucial for proper system assembly and resulting backlash. In the conducted experimentation, the output backlash ranged from near-zero to several degrees.

Next, the friction torque can be reduced. It would be possible in future iterations to significantly reduce the interference radius to decrease the friction torque. Halving the interference radius δr would yield, with the same springs, a variability of -14.0% to +35.0%.

The control of the blocking torque is not very precise, and one of the main assumptions is the characterization of the friction coefficient μ. This coefficient could be more accurately measured based on material nuances, treatments, and roughness. However, it seems challenging to achieve results with less than 20% variability [14]. Nevertheless, this does not compromise the functionality of the mechanism, as it is quite simple to ensure a sufficient blocking torque by slightly increasing the number of spring turns.

A misalignment effect between the spring and the ring has also been observed. This effect is presented in Figure 21. The misalignment is related to poor spring guidance, which can move slightly between axial stops. This phenomenon is more pronounced in springs with circular sections, as they provide less axial retention.

Test	a	b	c	d	e	A	B
Number of active turns N_a	2.24	2.24	2.24	2.24	2.24	3.24	3.24
Theoretical τ^b [N.mm] with μ = 0.2	707	707	707	707	707	2599	2599
Theoretical τ^b [N.mm] with μ = 0.15	327	327	327	327	327	910	910
Measured $\overline{\tau^b}$ [N.mm]	375	350	280	355	270	870	915

Table 5 Mean blocking torque of the non-backdrivable mechanism for different tests in the nominal configuration and by varying the number of turns

To address this issue, tighter tolerances can be employed to adjust the distance between the axial stops and the length of the spring.

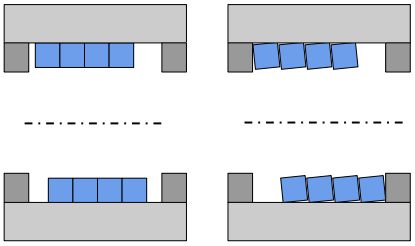

Fig. 21 Diagram of the spring misalignment effect during its rotation. On the left, the spring is mounted in its desired position. On the right, the spring misaligns.

Finally, the test bench can be improved by ensuring better coaxiality of the rotating elements. Moreover, replacing the static torque sensor upstream of the motor with a dynamic torque sensor downstream of the motor would enhance the measurement of the input torque.

6 Conclusions

This study proposes a new non-backdrivable mechanism suitable for myoelectric prostheses. This novel mechanism aims to be simpler and more cost-effective to manufacture, with a reduced number of components, while ensuring high efficiency to avoid oversizing the motorization.

A theoretical model has been proposed, and a dimensioning procedure allows adapting the system's dimensions to the specifications. A prototype has been designed, and experiments have been conducted to compare the theoretical model with the observed behavior. The measured values show a significant deviation from the expected values and need to be further validated. Nevertheless, the obtained results still demonstrate the potential of this mechanism. The residual friction torque can be low, enabling high efficiencies, and the blocking capability can be achieved with a relatively small number of spring turns.

Improvements can be made to reduce friction torque, limit the misalignment effect of the spring, and enhance measurement reliability. The next step involves integrating this mechanism into a power transmission chain to refine its integration and demonstrate the advantages of this type of mechanism.

Acknowledgment

The authors thank Lucie Michaud and Joseph-Jowel Sabin for their preliminary studies during their internship at Orthopus company and Nicolas Huchet for his valuable advice on the use of hand prostheses.

Funding Data

This research was supported by ANRT CIFRE grant n°2019 /1721 which funded the first author's doctoral studies. This research was supported by the project New smart and adaptive robotics solutions for personalized minimally invasive surgery in cancer treatment - ATHENA, funded by European Union – NextGenerationEU and Romanian Government, under National Recovery and Resilience Plan for Romania, contract no. 760072/23.05.2023, code CF 16/15.11.2022, through the Romanian Ministry of Research, Innovation and Digitalization, within Component 9, investment I8.

References

[1] Cordella, F., Ciancio, A. L., Sacchetti, R., Davalli, A., Cutti, A. G., Guglielmelli, E., and Zollo, L., 2016, "Literature Review on Needs of Upper Limb Prosthesis Users," Frontiers in Neuroscience, **10**.

[2] Butin, C., Chablat, D., Aoustin, Y., and Gouaillier, D., 2023, "Design of a Two-Speed Load Adaptive Variable Transmission for Energetic Optimization of an Accessible Prosthetic Hand," Journal of Mechanisms and Robotics, **15**(1), p. 011003.

[3] Belter, J. T., Segil, J. L., Dollar, A. M., and Weir, R. F., 2013, "Mechanical Design and Performance Specifications of Anthropomorphic Prosthetic Hands: A Review," The Journal of Rehabilitation Research and Development, **50**(5), pp. 599–618.

[4] Controzzi, M., Cipriani, C., and Carrozza, M. C., 2010, "Miniaturized Non-Back-Drivable Mechanism for Robotic Applications," Mechanism and Machine Theory, **45**(10), pp. 1395–1406.

[5] Controzzi, M., Bassi Luciani, L., and Montagnani, F., 2017, "Unified Approach to Bi-Directional Non-Back Drivable Roller Clutch Design," Mechanism and Machine Theory, **116**, pp. 433–450.

[6] "Projets: Bionicohand (accessed in August 2023)," https://bionico.org/cahier-des-charges-technical-specs/

[7] Butin, C., Chablat, D., Aoustin, Y., and Gouaillier, D., 2023, "Novel Kinematics of an Anthropomorphic Prosthetic Hand Allowing Lateral and Opposite Grasp With a Single Actuator," Journal of Computational and Nonlinear Dynamics, **18**(6), p. 061005.

[8] Plooij, M., Mathijssen, G., Cherelle, P., Lefeber, D., and Vanderborght, B., 2015, "Lock Your Robot: A Review of Locking Devices in Robotics," IEEE Robotics & Automation Magazine, **22**(1), pp. 106–117.

[9] Fanchon, J.-L., 2007, "Chapitre 31 : Engrenages - Efforts Sur Les Dentures," *Guides Des Sciences et Technologies Industrielles*, édition révisée ed., Nathan, pp. 365–372.

[10] Wiebusch, C. F., 1939, "The Spring Clutch," Journal of Applied Mechanics, **6**(3), pp. A103–A108.

[11] Wahl, A. M., 1940, "Discussion: "The Spring Clutch" (Wiebusch, C. F., 1939, ASME J. Appl. Mech., 6, Pp. A103–A108)," Journal of Applied Mechanics, **7**(2), pp. A89–A91.

[12] Budynas, R. G. and Sadegh, A. M., 2020, "Castigliano's Theorem, Chap 4.6," *Roark's Formulas for Stress and Strain*, 9th ed., New York: McGraw-Hill Education, pp. 83–89.

[13] Shigley, J., 2004, "Curved Beams and Rings," *Standard Handbook of Machine Design*, 3rd ed., The McGraw-Hill Companies, Inc., pp. 38.1–38.4.

[14] Cronin, K. and Gleeson, J. P., 2013, "Variability in Output Torque of Capstan and Wrap Spring Elements," Mechanism and Machine Theory, **68**, pp. 49–66.

List of Figures

List of Tables